Sensors & Diagnostics

PAPER

View Article Online
View Journal | View Issue

Cite this: *Sens. Diagn.*, 2026, **5**, 223

Enhancing wearable piezoelectric sensors *via* micro-textured P(VDF–TrFE)/$BaTiO_3$ nanofiber mats for physiological monitoring

Yan Xu,[a] Shiman Yang,[b] Cheng Liu,[b] Haoyu Wu,[c] Kaiping Huang,[c] Wenhui Xu,[c] Jiahe Wang*[a] and Yichun Ding *[bde]

Received 30th September 2025,
Accepted 31st October 2025

DOI: 10.1039/d5sd00175g

rsc.li/sensors

The advancement of wearable electronics for personalized healthcare demands flexible, high-performance pressure sensors capable of detecting both subtle physiological signals and large mechanical motions. In this work, we present a highly sensitive piezoelectric pressure sensor based on a micro-textured PVDF–TrFE/$BaTiO_3$ composite nanofiber mat, fabricated *via* a facile electrospinning process. A commercial paper napkin was employed as a template collector to directly imprint a micro-structured architecture onto the nanofiber mat, eliminating the need for complex processes. The addition of $BaTiO_3$ (BTO) nanoparticles significantly enhanced the piezoelectric response. The optimized piezoelectric sensor demonstrated outstanding performance with a sensitivity of ~197 mV kPa^{-1}, a fast response time of 3.5 ms, excellent frequency stability, and durability over 5000 loading cycles. Practical applicability was successfully verified through real-time monitoring of diverse physiological activities including arterial pulse, respiration, vocal vibrations, eye blinking, joint motion, and plantar pressure detection. These results underscore the potential of our sensor for use in wearable health monitoring, sports biomechanics, and human–machine interfaces, offering a scalable and cost-effective route to high-performance pressure sensing.

1. Introduction

The rise of the Internet of Things (IoT) and a growing focus on personalized health are driving innovation in wearable electronics.[1–4] These devices, which attach comfortably to the skin or are woven into fabrics, enable the continuous, real-time, and non-invasive collection of physiological signals.[5–8] This capability is transformative for fields like clinical diagnostics, remote patient monitoring, sports science, and human–machine interaction. Among the various sensing modalities, pressure sensors are especially critical. They convert mechanical stimuli from the body—from forceful joint movements to subtle pulses and muscle vibrations—into electrical signals.[9] By accurately detecting these signals, wearables can monitor vital signs, assess physical activity, recognize speech, and even track emotions. Therefore, developing high-performance, flexible pressure sensors is essential for next generation of wearable technology.

Pressure sensors can be primarily categorized into four types based on their operating mechanisms: piezoresistive, capacitive, piezoelectric, and triboelectric. Piezoresistive pressure sensors measure changes in electrical resistance, typically *via* compression of conductive composites or micro-cracked films.[10–13] They offer high sensitivity and simple readout but are plagued by hysteresis, high power consumption, and limited stability. Capacitive pressure sensors detect variations in capacitance between parallel electrodes when pressure alters their separation or the dielectric constant.[14,15] In particular, ionotronic pressure sensors have emerged as a sub-type capacitive pressure sensors that utilize electrical double layer (EDL) forms at the electrolyte/electrode interface within soft ion-conducting materials to achieve high sensitivity.[16] These excel in power efficiency, response speed, and static stability, though they are vulnerable to electromagnetic interference and often require shielding. Triboelectric pressure sensors generate voltage through contact electrification and electrostatic induction during physical contact and separation.[17–22] Their key advantages include self-powering operation and high output voltage, but they are restricted to dynamic pressure sensing and suffer from output inconsistency due to environmental factors like humidity. In contrast, piezoelectric

[a] *Department of Family Medicine, Shengjing Hospital of China Medical University, Shenyang, 110022, China. E-mail: wangjiahe_sj@126.com*
[b] *School of Physics and Materials Science, Nanchang University, Nanchang, 330031, China*
[c] *School of Pharmacy, Jiangxi University of Chinese Medicine, Nanchang, 330004, China*
[d] *Jiangxi Provincial Key Laboratory of Photodetectors, Nanchang University, Nanchang 330031, China*
[e] *Research Center for Chip Design, Nanchang University, Nanchang 330031, China. E-mail: yichun.ding@ncu.edu.cn*

pressure sensors produce an inherent charge in response to mechanical strain without requiring external power, enabling fast response, superior dynamic signal detection, and low-power operation.[23,24] These traits make them ideally suited for capturing transient physiological signals, such as pulse, voice, and motion, in wearable applications.[25]

Despite their considerable promise, the development of high-performance flexible piezoelectric pressure sensors faces several key challenges. A primary obstacle is achieving high sensitivity to capture faint physiological signals, while also ensuring the device exhibits excellent mechanical flexibility and durability to endure repeated bending, stretching, and compression during daily use. In the search for suitable materials, piezoelectric polymers and composites have attracted significant attention due to their intrinsic flexibility and processability, offering distinct advantages over rigid, brittle ceramics such as barium titanate ($BaTiO_3$) or lead zirconate titanate (PZT). Among these, poly(vinylidene fluoride) (PVDF) and its copolymers (*e.g.*, PVDF–TrFE) have become leading candidates for flexible piezoelectric sensors.[26,27] Their strong piezoelectric properties originate from the polar β-phase crystalline structure. PVDF–TrFE, in particular, holds an advantage over PVDF homopolymer by forming the electroactive β-phase directly from solution or melt,[28–30] bypassing the need for mechanical stretching and thus simplifying production while improving piezoelectric performance. Combined with its high chemical stability, biocompatibility, and reliable film-forming ability, PVDF–TrFE serves as an ideal material for creating soft, conformable, and high-output piezoelectric pressure sensors.

Electrospinning has proven to be an effective technique for fabricating piezoelectric nanofibers from PVDF and its copolymers for making flexible pressure sensors.[31–33] The process involves the uniaxial stretching of a polymer jet under a high-voltage electric field, which promotes the alignment of molecular dipoles and induces a high concentration of the piezoelectric β-phase.[34] The resulting non-woven mats of nanofibers possess a highly porous, fibrous architecture that is inherently more deformable under low pressure than solid films, leading to a greater piezoelectric output for a given force. Additionally, piezoelectric nanoparticles like $BaTiO_3$ can be incorporated into the fibers to further improve piezoelectric performance.[35–38] However, a key limitation of conventional flat, non-woven electrospun mats is their limited compressibility. While they are sensitive to small forces, their dense, randomly oriented fiber networks can quickly reach a compression saturation point, limiting their sensitivity and dynamic range for higher pressures. To overcome this drawback and further amplify sensitivity, researchers have explored micro-structuring the active layer. By creating well-defined micropatterns (*e.g.*, domes, and pyramids) on the sensor surface, the applied pressure is concentrated onto the protruding features.[39–42] This architecture dramatically increases the local stress and strain within the material at the points of contact, leading to a significantly higher piezoelectric charge generation compared to a flat film under the same pressure. Although this strategy significantly enhances sensitivity, creating such micropatterns often involves complex fabrication techniques.

In this work, we developed a highly sensitive, flexible piezoelectric pressure sensor based on a micro-textured nanofibrous composite mat for wearable physiological signal monitoring. The active layer is composed of electrospun nanofibers of a P(VDF–TrFE) co-polymer matrix embedded with barium titanate ($BaTiO_3$, BTO) nanoparticles. Crucially, we employ a facile and efficient single-step electrospinning process using a commercial paper napkin as a template collector to directly fabricate a well-ordered micro-textured architecture on the nanofiber mat. This method eliminates the need for complex post-processing or lithography, offering a simple and scalable route to high-performance sensing layers. We investigated the critical fabrication parameters, including the BTO nanoparticle filling content and the mat thickness, to optimize the material's properties. The morphology, crystalline structure, and chemical composition of the developed micro-textured P(VDF–TrFE)/BTO composite fibers were thoroughly characterized. The pressure sensing performance of the fabricated device, including its sensitivity, response time and durability, was evaluated. Finally, the practical utility of our sensor was convincingly demonstrated through its successful application in capturing a wide range of human physiological signals, including radial artery pulse waves, respiration, vocal cord vibrations for speech recognition, subtle eye blinking motions, and various gross motor activities such as wrist bending and walking. This work provides an effective strategy for manufacturing high-output, flexible piezoelectric sensors, paving the way for their use in sophisticated health monitoring and human–machine interaction systems.

2. Experimental

2.1 Materials

Polyvinylidene fluoride–trifluoroethylene (PVDF–TrFE, 7/3, M_w: 45000) was purchased from Piezotech (France). $BaTiO_3$ (BTO) particles (< 1 μm, 99.5%) and *N*,*N*-dimethylformamide (DMF, AR, ≥99.5%) were purchased from Aladdin (Shanghai). Acetone (AR, ≥99.5%) was purchased from Sinopharm Chemical Reagent Co., Ltd.

Preparation of PVDF–TrFE/BTO composite nanofibers. PVDF–TrFE/BTO solutions were prepared by first dispersing BTO nanoparticles in a mixture solvent of DMF and acetone (7 : 3 by mass) using 30 minutes of sonication. PVDF–TrFE powder was then added to the suspension and stirred overnight at 60 °C in a water bath to achieve complete dissolution. The concentration of PVDF–TrFE was maintained at 16 wt%, while the BTO content was varied at 0, 10, 15, 20, 25, and 30 wt% relative to PVDF–TrFE. The obtained PVDF–TrFE/BTO solutions were subsequently used for electrospinning. In particular, a 4 mL solution was loaded into a syringe equipped with an 18-gauge metal

needle. Electrospinning was carried out at an applied voltage of 16–18 kV and a solution feed rate of 1 mL h^{-1}. For collecting the nanofibers, either flat aluminium foil or a textured paper napkin was wrapped around a rotating drum to produce flat and micro-textured nanofiber mats, respectively. The drum had a diameter of 10 cm and a width of 20 cm, and it rotated at approximately 50 rpm. Finally, the electrospun PVDF–TrFE/BTO composite nanofiber mats were vacuum-dried at 60 °C to ensure complete removal of residual solvent.

2.2 Characterization

The morphological features of the electrospun P(VDF–TrFE)/BTO nanofiber mats were examined using a field emission scanning electron microscope (FE-SEM, ZEISS GeminiSEM 300). The internal structure and dispersion of BTO nanoparticles within the nanofibers were further investigated by high-resolution transmission electron microscopy (HR-TEM, JEOL JEM-F200), coupled with energy-dispersive X-ray spectroscopy (EDS) for elemental analysis. Crystalline structure was analysed by X-ray diffraction (XRD) on a Bruker D8 ADVANCE diffractometer. Chemical functional groups were characterized using a Thermo Scientific Nicolet iS50 FT-IR spectrophotometer equipped with an attenuated total reflection (ATR) accessory. Thermal stability was evaluated *via* thermogravimetric analysis (TGA) on a Mettler Toledo TGA/DSC3+ instrument, with samples heated from 30 °C to 800 °C at a rate of 10 °C min^{-1} under a nitrogen atmosphere. Mechanical properties were assessed through uniaxial tensile testing performed on a universal testing machine. Specimens of the micro-textured nanofiber mats were cut into 5 mm × 40 mm strips and tested at a crosshead speed of 30 mm min^{-1}. The initial gauge length was set at about 30 mm. Three replicates were measured for each sample type to ensure statistical significance.

2.3 Pressure sensor assembly and performance tests

A piezoelectric pressure sensor was constructed by sandwiching a P(VDF–TrFE)/BTO nanofiber mat between two Au/PET electrodes (1.0 × 1.0 cm) and sealing the assembly with adhesive tape. The PET/Au electrodes were prepared by successive evaporation of Cr (5 nm) and Au (100 nm) layers onto a 20 μm PET film *via* thermal evaporation. The sensor was subjected to forces of varying magnitudes and frequencies using a universal testing machine, and the output voltage was recorded with an oscilloscope (Tektronix TBS 1000C). The size of the indenter was about 0.5 × 0.5 cm. To evaluate durability, the sensor was subjected to 5000 cyclic loading tests using an oscillator, while the long-term electrical output was monitored with an electrometer (Keithley 6517B).

2.4 Physiological signal detection

All experiments were performed in accordance with the institutional guidelines (SYKX-2021-0004) and approved by the ethics committee at Nanchang University. Informed consent was obtained from the human participant.

The flexible piezoelectric pressure sensor was deployed on various locations of the human body to monitor a range of physiological activities and mechanical signals, including arterial pulse, respiration, vocal cord vibrations, eye blinking, joint bending, and plantar pressure during gait. For instance, in arterial pulse measurements, the sensor was affixed over the radial artery on the ventral side of the wrist using medical tape. The resulting output signals were recorded with an electrometer. Similarly, the sensor was mounted at appropriate anatomical sites to capture other signals: near the nose for respiratory monitoring, on the throat for detecting vocal vibrations during speech, adjacent to the eye for recording blink motions, on the wrist for monitoring joint flexion, and beneath the sole of the foot to measure plantar pressure during walking.

3. Results and discussion

3.1 Design and fabrication of the micro-textured PVDF–TrFE/BTO composite nanofiber mat

Fig. 1a schematically illustrates the fabrication process of the micro-textured PVDF–TrFE/BTO composite nanofiber mat *via* electrospinning. During this process, a high DC voltage is applied to eject polymer nanofibers from the needle, during which the molecular chains are stretched under electrostatic forces. The nanofibers are deposited onto a collector to form a nonwoven mat, whose fiber diameter and overall thickness can be controlled by adjusting electrospinning parameters such as voltage, solution feed rate, and volume. Conventionally, a flat aluminium foil is employed as the collector, which results in a flat nanofiber mat. Herein, in this study, we utilized a commercial paper napkin with intrinsic micropatterns as the collector to produce a micro-textured fiber mat. Paper napkins typically feature embossed patterns for improved functionality (*e.g.*, absorbency) and visual appeal. As shown in Fig. 1b, the napkin used herein exhibits distinct micro-dome patterns. During electrospinning, the PVDF–TrFE/BTO nanofibers conform to this micro-textured surface, faithfully replicating the patterns onto the resulting fiber mat.

The resulting PVDF–TrFE/BTO composite nanofiber mat has a thickness of approximately 30 μm and exhibits excellent flexibility (Fig. 1c). Fig. 1d clearly shows the replicated micropatterns, which match the size and morphology of the original napkin, confirming successful pattern transfer. SEM imaging further reveals the presence of micro-grooves on the fiber mat inherited from the napkin collector (Fig. 1e), and shows that the PVDF–TrFE/BTO nanofibers are continuous with certain BTO nanoparticles exposed on the surface of the nanofibers (Fig. 1f). This flexible composite fiber mat can be cut into desired dimensions for sensor assembly. As depicted in Fig. 1g, a piezoelectric pressure sensor was fabricated by sandwiching the nanofiber mat between two Au/PET electrodes. The

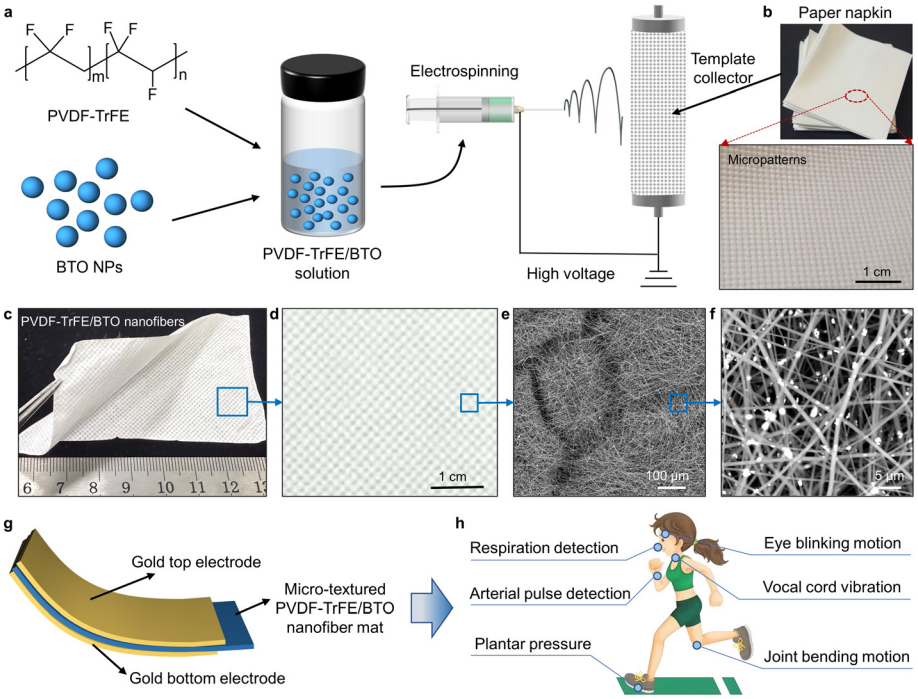

Fig. 1 (a) Schematic illustration of the fabrication of the micro-textured PVDF–TrFE/BTO composite nanofiber mat by electrospinning using a paper napkin as a collector. (b) Optical image of the paper napkin, where micropatterns can be easily identified. (c and d) Optical images of the as-fabricated flexible micro-textured PVDF–TrFE/BTO composite nanofiber mat, where patterns were duplicated from the napkin. (e and f) SEM images of the micro-textured PVDF–TrFE/BTO composite nanofiber mat. (g) Schematic illustration of the assembly of flexible piezoelectric sensors by sandwiching the PVDF–TrFE/BTO nanofiber mat between top and bottom Au electrodes. (h) Schematic illustration of applying the piezoelectric pressure sensors for versatile wearable applications.

resulting device is highly conformable and suitable for attachment to various parts of the human body to monitor physiological signals including arterial pulse, respiration, vocal vibrations, eye blinking, joint motion, and plantar pressure during walking (Fig. 1h).

3.2 Characterization of the PVDF–TrFE/BTO composite nanofiber mat

The morphological characteristics of the electrospun nanofibers were thoroughly investigated using scanning electron microscopy (SEM). As illustrated in Fig. 2a, the nanofibers composed of pure PVDF–TrFE exhibited a uniform and smooth morphology with no visible surface defects. In contrast, the incorporation of BTO nanoparticles resulted in the presence of surface protrusions and aggregates of BTO. The density and prominence of these surface features showed a clear positive correlation with increasing BTO content. Although the electrospinning process is generally expected to fully encapsulate filler nanoparticles within the polymer matrix, a reduction in the composite fiber diameter can result in the partial exposure of BTO on the surface, making them externally visible. A further surface modification of the BTO nanoparticles may improve

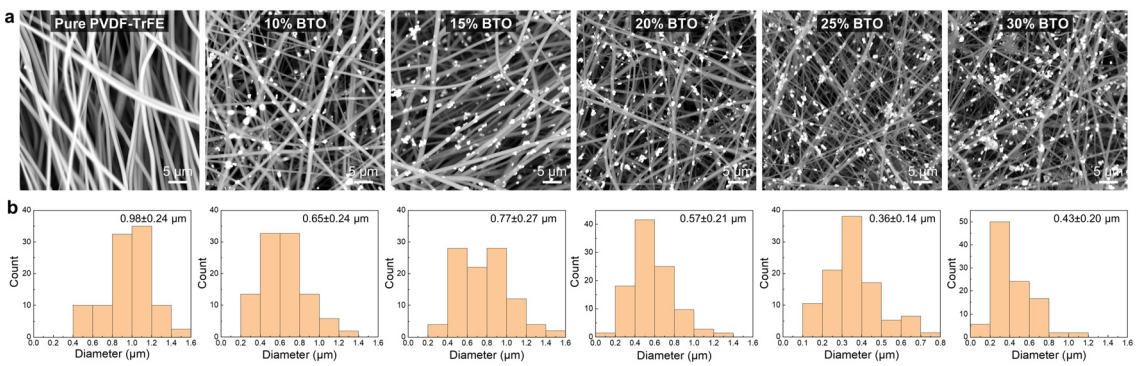

Fig. 2 SEM images (a) and corresponding fiber diameter statistics (b) of pure PVDF–TrFE nanofibers and PVDF–TrFE/BTO composite nanofibers with a BTO content of 10, 15, 20, 25, and 30%, respectively.

the uniform dispersion of BTO and mitigate the aggregates. Quantitative analysis of the SEM images determined the average diameter of the pure PVDF–TrFE nanofibers to be approximately 980 nm (Fig. 2b). The addition of BTO nanoparticles induced a measurable decrease in the average fiber diameter. This thinning effect is likely attributable to the enhanced dielectric permittivity of the polymer solution with BTO, which facilitates greater jet stretching under the applied electric field, compounded by the use of a slightly higher electrospinning voltage. The successful incorporation of BTO nanoparticles was further confirmed by transmission electron microscopy (TEM) and energy-dispersive X-ray spectroscopy (EDS) elemental mapping. Fig. 3 shows that nanoparticles are embedded in nanofibers, and the Ba and Ti elements are uniformly distributed within a single nanofiber, verifying the presence of BTO.

The crystalline structure of the nanofibers was characterized using X-ray diffraction (XRD). As shown in Fig. 4a, the pure PVDF–TrFE nanofibers exhibited a broad peak at approximately 2θ = 20.2°, which corresponds to the reflection of the β-phase crystal structure of PVDF–TrFE.[43,44] This characteristic β-phase peak remained present in all PVDF–TrFE/BTO composite samples after the incorporation of BTO nanoparticles. In addition, distinct crystalline peaks attributable to BTO were clearly observed and were found to perfectly match the reference pattern for BTO (PDF#31-0174).[45] Moreover, the intensity of the BTO diffraction peaks exhibited an increasing trend with higher BTO content. We further evaluated the β-phase crystalline structure of PVDF–TrFE using Fourier transform infrared (FTIR) spectroscopy. As shown in Fig. 4b, all samples exhibited a distinct characteristic peak near 840 cm^{-1}, corresponding to the β-phase, while only a negligible peak was observed for the α-phase at approximately 760 cm^{-1}.[46,47] The high content of the β-phase can be attributed to the electrospinning process, which promotes polarization under a high electric field and facilitates molecular stretching. Therefore, the high β-phase content, combined with the incorporation of BTO nanoparticles, is expected to enhance the piezoelectric performance.

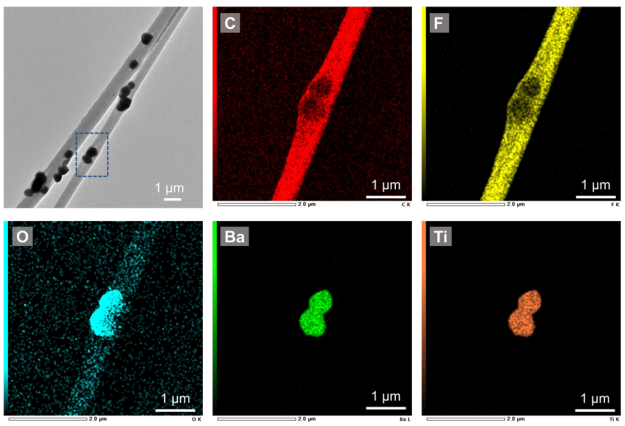

Fig. 3 TEM image and EDS elemental mappings of PVDF–TrFE/BTO composite nanofibers.

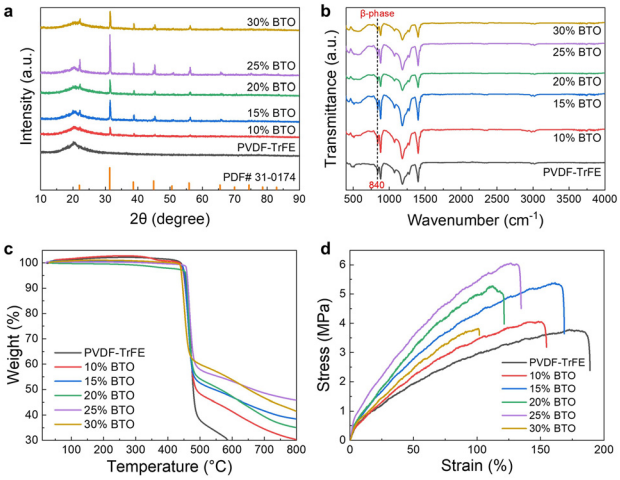

Fig. 4 (a) XRD patterns of pure PVDF–TrFE nanofibers and PVDF–TrFE/BTO composite nanofibers. (b) FT-IR spectra of pure PVDF–TrFE nanofibers and PVDF–TrFE/BTO composite nanofibers. (c) TGA curves of pure PVDF–TrFE nanofibers and PVDF–TrFE/BTO composite nanofibers under a nitrogen atmosphere. (d) Representative tensile stress–strain curves of the pure PVDF–TrFE nanofiber mat and PVDF–TrFE/BTO composite nanofiber mats.

The thermal stability of the PVDF–TrFE/BTO nanofibers was evaluated using thermogravimetric analysis (TGA). As depicted in Fig. 4c, all samples exhibited decomposition temperatures above 400 °C under a nitrogen atmosphere, demonstrating their good thermal stability. Furthermore, the residual mass (char yield) increased with higher BTO content, confirming the successful and increased incorporation of BTO nanoparticles. Mechanical properties are critical for practical applications. As shown in Fig. 4d, the tensile strain was not significantly affected by the inclusion of BTO nanoparticles. Even at a high BTO loading of 30%, the tensile strain remained above 100%. In addition, the tensile stress showed a continuous increase with BTO content up to 25%. These results indicate that the PVDF–TrFE/BTO composite nanofiber mats possess both excellent mechanical strength and sufficient flexibility, making them suitable for wearable applications.

3.3 Piezoelectric pressure sensing properties of the PVDF–TrFE/BTO nanofiber mat

We assembled piezoelectric pressure sensors by sandwiching the P(VDF–TrFE)/BTO nanofiber mat between two Au/PET electrodes (1.0 × 1.0 cm^2) and sealing the assembly with adhesive tape. The output performance of sensors made from flat and micro-textured P(VDF–TrFE)/BTO nanofiber mats was compared (Fig. 5a). Results showed that the micro-textured fiber mat generated a significantly higher output voltage under the same compression force. Specifically, the micro-textured fiber mat produced an output voltage of approximately 1.65 V, whereas the flat mat yielded only 0.5 V.

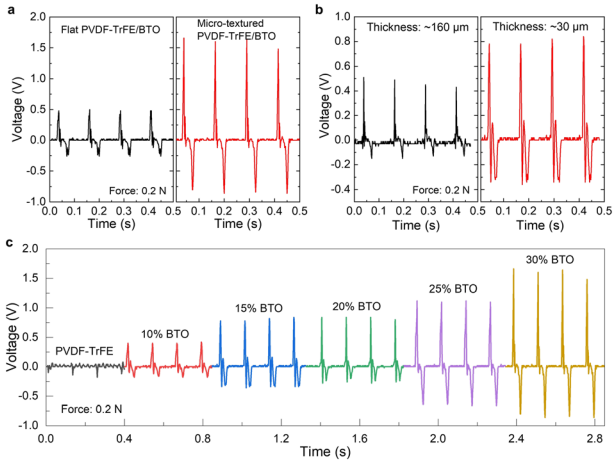

Fig. 5 (a) Comparison of output voltage from piezoelectric pressure sensors made from the flat and micro-textured PVDF–TrFE/BTO (30%) nanofiber mat. (b) Comparison of output voltage from piezoelectric pressure sensors made from micro-textured PVDF–TrFE/BTO (20%) with different thicknesses (160 and 30 μm). (c) Typical output voltage of piezoelectric pressure sensors made from the micro-textured PVDF–TrFE/BTO nanofiber mat with different BTO contents.

This notable enhancement in piezoelectric performance can be attributed to the micro-grooved structure of the fiber mat, which promotes greater stress concentration and deformation, along with the well-developed crystalline β-phase structure. We then investigated the influence of fiber mat thickness on output performance. Compared to the thinner sample (30 μm), the thicker PVDF–TrFE/BTO fiber mat (160 μm) exhibited a much lower output voltage (Fig. 5b). This reduction is likely due to the higher porosity and less distinct micro-textured morphology in thicker mats, which may hinder efficient stress transfer and reduce overall piezoelectric response. Therefore, a thinner mat with a thickness of 30 μm was selected for subsequent experiments. Finally, the effect of BTO nanoparticle content on the output performance was evaluated (Fig. 5c). The output voltage increased gradually with higher BTO content, confirming that the incorporation of BTO nanoparticles effectively enhances the piezoelectric effect of the nanofiber mat, thereby improving the sensitivity of the pressure sensors.

Fig. 6a presents the typical output voltage response of a piezoelectric pressure sensor fabricated from the micro-textured PVDF–TrFE/BTO (30%) nanofiber mat, measured under compression forces ranging from 0.02 N to 0.2 N. The pressure sensor exhibited a linearly increasing output voltage with applied force, demonstrating a pressure sensitivity of approximately 7.87 V N^{-1}, equivalent to ~197 mV kPa^{-1}. The sensitivity is higher than most of the reported piezoelectric pressure sensors based on electrospun PVDF-based nanofibers (Table 1). As illustrated in Fig. 6b, the sensor was also subjected to a constant compressive force applied at varying frequencies. The output amplitude remained consistent across the frequency range tested, indicating minimal frequency dependence within the evaluated spectrum. Furthermore, the sensor demonstrated a rapid response time of approximately 3.5 ms (Fig. 6c), highlighting its capability for detecting dynamic mechanical stimuli. In addition to its dynamic performance, the device exhibited

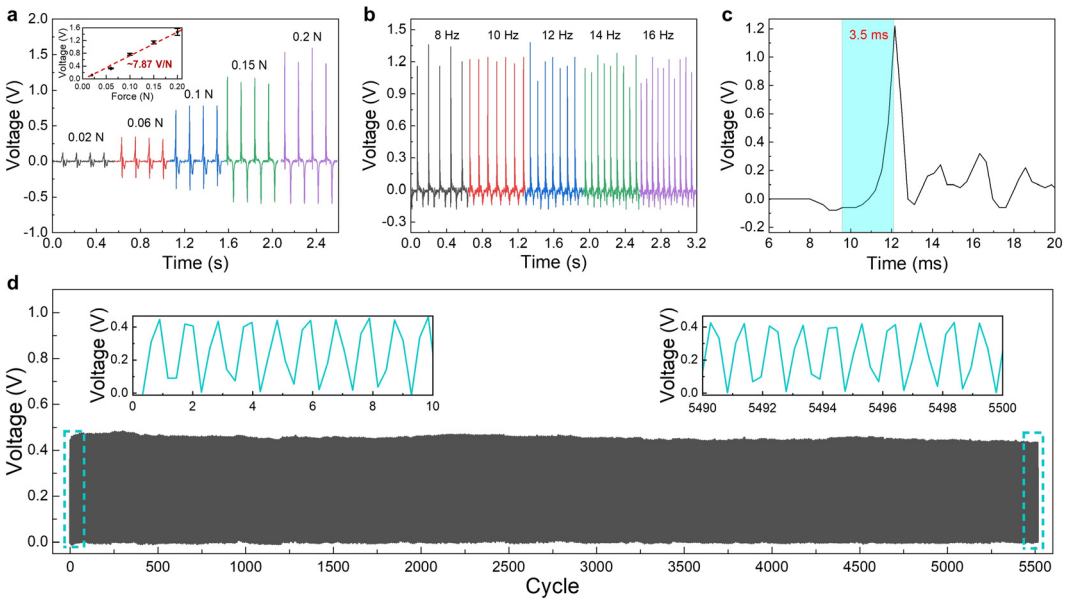

Fig. 6 (a) Typical output voltage of a piezoelectric pressure sensor made from the micro-textured PVDF–TrFE/BTO (30%) nanofiber mat under varying compression forces. The inset plots the corresponding maximum output voltage as a function of the applied force, revealing a sensitivity of approximately 7.87 V N^{-1} (~197 mV kPa^{-1}). (b) Typical output voltage of a piezoelectric pressure sensor made from the micro-textured PVDF–TrFE/BTO (30%) nanofiber mat under different frequencies at a constant force. (c) Zoomed-in output voltage profile of the piezoelectric sensor, illustrating its response time. (d) Output voltage profile of the piezoelectric sensor over 5000 loading/unloading cycles at a constant force. Insets show the initial and last 10 cycles, respectively.

Table 1 Comparison of the sensing performance of electrospun PVDF nanofiber-based piezoelectric pressure sensors

Sample	Fabrication method	Sensitivity	Pressure range	Ref
PVDF nanofibers	Electrospinning	~23.3 mV kPa^{-1}	36.67–102.62 kPa	48
PVDF/BTO membrane	Near-field electrospinning	73 mV N^{-1}	2–70 N	38
PVDF/PZT nanofibers	Electrospinning	173.5 mV N^{-1}	—	49
PVDF/GO nanofibers	Electrospinning	38.8 mV N^{-1}	20–65 kPa	50
PVDF–TrFE/MXene nanofibers	Electrospinning	79 mV N^{-1}	20 N	51
PVDF/rGO nanofibers	Electrospinning	19.09 kPa^{-1}	1–25 kPa	52
PVDF–TrFE /$BaTiO_3$/MXene	Electrospinning	—	0.2–400 kPa	35
Micro-texture PVDF/BTO nanofibers	Template electrospinning	7.87 V N^{-1} (197 mV kPa^{-1})	0.02–0.2 N	This work

excellent operational durability, maintaining stable output over 5000 continuous loading–unloading cycles with negligible signal attenuation or variation (Fig. 6d). These results collectively affirm that the piezoelectric pressure sensor made from the micro-textured PVDF–TrFE/BTO composite nanofiber mat possesses high linearity, rapid response, and remarkable stability, making it a promising candidate for use in practical wearable sensing applications.

3.4 Wearable applications of PVDF–TrFE/BTO nanofiber-based pressure sensors

We applied the micro-textured PVDF–TrFE/BTO nanofiber-based flexible piezoelectric pressure sensor at various locations on the human body to assess its performance in detecting diverse physiological activities and mechanical signals. As illustrated in Fig. 7, the device exhibited high sensitivity and reliable operation across multiple applications including arterial pulse monitoring, respiration detection, vocal vibration sensing, eye blink tracking, joint motion measurement, and gait analysis.

First, we affixed the sensor to the ventral wrist, which achieved clear acquisition of arterial pulse waveforms (Fig. 7a). When positioning the sensor near the nasal orifice, it allowed consistent detection of respiratory cycles through rhythmic pressure variations during inhalation and exhalation (Fig. 7b). Furthermore, we mounted the sensor on the throat; it can distinguish vocal vibrations corresponding to specific words such as "sensor" (Fig. 7c), demonstrating its potential for wearable speech recognition applications.

In motion detection, the sensor can effectively capture both subtle and large-scale movements. By placing the sensor near the orbital region, it can measure signals corresponding to eye blinking activity (Fig. 7d). Then, we secured the sensor to the dorsal wrist and subjecting it to controlled bending angles of 20°, 40°, and 60°. The output voltage increased proportionally with bending angle (Fig. 7e), confirming the sensor's ability to quantify joint movement for rehabilitation and sports science applications. Finally, we achieved consistent recording of plantar pressure signals across different walking frequencies by embedding the sensor within a shoe insole (Fig. 7f), demonstrating its frequency stability and durability under dynamic loading conditions. These findings highlight the potential of this technology for continuous health monitoring, sports biomechanics, and personalized medical diagnostics. Noting that a baseline drift

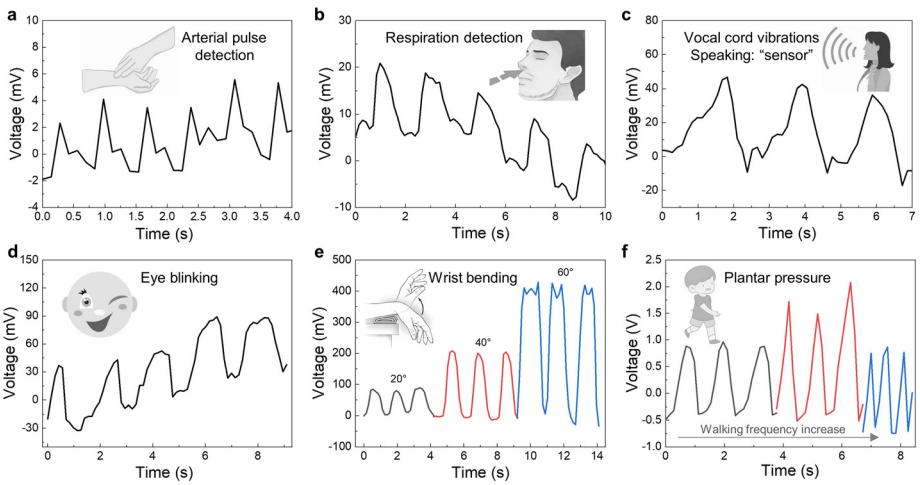

Fig. 7 (a) Detection of arterial pulse by affixing a pressure sensor to the ventral wrist surface over the radial artery with medical tape. (b) Human respiratory monitoring by positioning a pressure sensor near the nasal orifice. (c) Speech recognition through detection of acoustic-mechanical vibrations during vocalization (*e.g.*, pronouncing the word "sensor") by mounting a pressure sensor on the throat. (d) Eye-blink motion detection by placing a pressure sensor near the orbital region. (e) Monitoring wrist flexion by securing a pressure sensor onto the dorsal side of the wrist. (f) Plantar pressure detection during human walking by embedding a pressure sensor within the shoe insole.

was observed in some applications, which is attributed to environmental fluctuations such as skin temperature. This is a common challenge in skin-attached electronics that can be mitigated through algorithmic compensation and material or structural optimization.

Conclusions

In this study, we successfully developed a highly sensitive, flexible piezoelectric pressure sensor based on a micro-textured PVDF–TrFE/BTO composite nanofiber mat for multifunctional wearable sensing applications. The sensor was fabricated *via* a facile and scalable electrospinning process using a commercially available patterned paper napkin as a collector, which enabled the direct formation of a micro-textured architecture without complex post-processing. The incorporation of BTO nanoparticles significantly enhanced the piezoelectric performance, while the optimized nanofiber morphology and β-phase crystalline structure contributed to high sensitivity and mechanical robustness. The resulting sensor exhibited outstanding performance, including a high sensitivity of ~197 mV kPa^{-1}, a fast response time of 3.5 ms, excellent frequency stability, and remarkable durability over 5000 loading cycles. The practical utility of the sensor was demonstrated through its successful deployment in monitoring a wide range of physiological signals and body motions, including arterial pulse waveforms, respiratory rhythms, vocal vibrations, eye blinks, wrist flexion at varying angles, and plantar pressure during gait. These results highlight the sensor's ability to capture both subtle physiological activities and larger-scale biomechanical movements with high fidelity, underscoring its versatility for use in health monitoring, sports science, and human–machine interfaces. This work provides a cost-effective and scalable strategy for manufacturing high-performance piezoelectric sensors with micro-engineered surface structures. The proposed sensor platform shows great promise for continuous, real-time monitoring in wearable electronics, and future efforts will focus on integration into wireless systems and validation in clinical and field settings for personalized healthcare applications.

Author contributions

Conceptualization, Y. X., J. W. and Y. D.; methodology, Y. X., S. Y., C. L., H. W., and K. H.; software, Y. X. and S. Y.; validation, Y. X., S. Y., C. L., H. W., and K. H.; formal analysis, Y. X. and S. Y.; investigation, Y. X., S. Y. and C. L.; resources, J. W. W. X. and Y. D.; data curation, Y. X. and S. Y.; writing – original draft preparation, Y. X.; writing – review and editing, J. W. and Y. D.; visualization, Y. X. and S. Y.; supervision, J. W. and Y. D.; project administration, J. W. W. X. and Y. D.; funding acquisition, J. W., W. X. and Y. D. All authors have read and agreed to the published version of the manuscript.

Conflicts of interest

There are no conflicts to declare.

Data availability

This manuscript is complete as submitted, and all supporting data are presented within the main text and figures.

Acknowledgements

This research was funded by the Shenyang Science and Technology Plan Project (24-214-3-162), the National Science Foundation of China (62461042 and 52163002), the Jiangxi Provincial Natural Science Foundation (20252BAC240694), the Jiangxi Provincial Key Laboratory of Photodetectors (2024SSY03041), Jiangxi University of Chinese Medicine Science and Technology Innovation Team Development Program (CXTD22002), and the start-up funding of Nanchang University (28170137).

References

1 G. Chen, X. Xiao, X. Zhao, T. Tat, M. Bick and J. Chen, *Chem. Rev.*, 2022, **122**, 3259–3291.
2 M. Stoppa and A. Chiolerio, *Sensors*, 2014, **14**, 11957–11992.
3 Y. Ding, J. Jiang, Y. Wu, Y. Zhang, J. Zhou, Y. Zhang, Q. Huang and Z. Zheng, *Chem. Rev.*, 2024, **124**, 1535–1648.
4 X. He, Z. Li, X. Huang, Q. Zhang, Y. Zeng, J. Li, C. K. Yiu, Y. Yang, J. Zhou, G. Xu, J. Wang, J. Li, Z. Xu, Z. Chen, Y. Liu, Y. Gao, B. Zhang, G. Zhao, Z. Gao, P. Wu, R. Shi, Y. Qiu, H. Zhang, L. Chow, D. Ye, Y. Huang and X. Yu, *BMEMat*, 2025, **3**, e12124.
5 X. Wang, Z. Liu and T. Zhang, *Small*, 2017, **13**, 1602790.
6 J. Jiang, X. Song, Y. Qi, X. Tao, Z. Zheng and Q. Huang, *Adv. Fiber Mater.*, 2025, **7**, 894–907.
7 D. Kim, J. Min and S. H. Ko, *Adv. Sens. Res.*, 2024, **3**, 2300118.
8 F. Guo, Z. Ren, S. Wang, Y. Xie, J. Pan, J. Huang, T. Zhu, S. Cheng and Y. Lai, *Nano-Micro Lett.*, 2025, **17**, 302.
9 Y. Ding, T. Xu, O. Onyilagha, H. Fong and Z. Zhu, *ACS Appl. Mater. Interfaces*, 2019, **11**, 6685–6704.
10 Y. Ding, J. Yang, C. R. Tolle and Z. Zhu, *ACS Appl. Mater. Interfaces*, 2018, **10**, 16077–16086.
11 T. Xu, Y. Ding, Z. Wang, Y. Zhao, W. Wu, H. Fong and Z. Zhu, *J. Mater. Chem. C*, 2017, **5**, 10288–10294.
12 H. Yuan, X. Liao, K. Wu, J. Chen, K. Chen, T. Zhu, Y. Wang, J. Zhang, G. Liu and J. Sun, *Adv. Mater. Interfaces*, 2023, **10**, 2202169.
13 C. Song, J. Liu, Y. Cao, W. Li and C. He, *Langmuir*, 2024, **40**, 20515–20525.
14 R. B. Mishra, N. El-Atab, A. M. Hussain and M. M. Hussain, *Adv. Mater. Technol.*, 2021, **6**, 2001023.
15 D. Guo, Y. Li, Q. Zhou, Z. Yu, X. Liu, S. Dong, S. Zhang, H.-K. Sung, Z. Yao, Y. Li and Y. Li, *Nano Energy*, 2024, **127**, 109750.

16 Y. Li, N. Bai, Y. Chang, Z. Liu, J. Liu, X. Li, W. Yang, H. Niu, W. Wang, L. Wang, W. Zhu, D. Chen, T. Pan, C. F. Guo and G. Shen, *Chem. Soc. Rev.*, 2025, **54**, 4651–4700.
17 X. Xiong, J. Liang and W. Wu, *Nano Energy*, 2023, **113**, 108542.
18 Y. Qi, J. Jiang, F. Chen, J. Zhou, J. Liang, J. Fu, Y. Yang, Y. Ding, Z. Zheng and Q. Huang, *Small*, 2025, **21**, 2504556.
19 F. Chen, X. Song, J. Fu, J. Liang, J. Zhou, J. Cai, Y. Zhang, M. Zhu, Y. Ding, J. Jiang, Z. Chen, Y. Qi, Z. Zhou, Q. Huang, Y. Zhang and Z. Zheng, *J. Mater. Chem. A*, 2024, **12**, 30298–30308.
20 L. Zhao, S. Y. Wong, J. Y. Sim, J. Zhou, X. Li and C. Wang, *BMEMat*, 2023, **1**, e12020.
21 Q. Zheng, X. Dai, Y. Wu, Q. Liang, Y. Wu, J. Yang, B. Dong, G. Gao, Q. Qin and L.-B. Huang, *BMEMat*, 2023, **1**, e12008.
22 Y. Zhang, J. Fu, Y. Ding, A. A. Babar, X. Song, F. Chen, X. Yu and Z. Zheng, *Adv. Mater.*, 2024, **36**, 2311633.
23 D. B. Kim, J. Han, S. M. Sung, M. S. Kim, B. K. Choi, S. J. Park, H. R. Hong, H. J. Choi, B. K. Kim, C. H. Park, J. H. Paik, J.-S. Lee and Y. S. Cho, *npj Flexible Electron.*, 2022, **6**, 69.
24 K. Jeronimo, V. Koutsos, R. Cheung and E. Mastropaolo, *Sensors*, 2021, **21**, 5873.
25 C. Zhi, S. Shi, Y. Si, B. Fei, H. Huang and J. Hu, *Adv. Mater. Technol.*, 2023, **8**, 2201161.
26 F. Qi, L. Xu, Y. He, H. Yan and H. Liu, *Cryst. Res. Technol.*, 2023, **58**, 2300119.
27 M. Zhu, S. S. Chng, W. Cai, C. Liu and Z. Du, *RSC Adv.*, 2020, **10**, 21887–21894.
28 X. Yuan, X. Gao, X. Shen, J. Yang, Z. Li and S. Dong, *Nano Energy*, 2021, **85**, 105985.
29 H. Abdolmaleki, A. B. Haugen, K. B. Buhl, K. Daasbjerg and S. Agarwala, *Adv. Sci.*, 2023, **10**, 2205942.
30 A. Ahmed, Y. Jia, H. Deb, M. F. Arain, H. Memon, K. Pasha, Y. Huang, Q. Fan and J. Shao, *J. Mater. Sci.: Mater. Electron.*, 2022, **33**, 3965–3981.
31 X. Wang, F. Sun, G. Yin, Y. Wang, B. Liu and M. Dong, *Sensors*, 2018, **18**, 330.
32 X. Wan, H. Cong, G. Jiang, X. Liang, L. Liu and H. He, *ACS Appl. Nano Mater.*, 2023, **6**, 1522–1540.
33 S. Zhang, B. Zhang, J. Zhang and K. Ren, *ACS Appl. Mater. Interfaces*, 2021, **13**, 32242–32250.
34 X. Liu, S. Xu, X. Kuang, D. Tan and X. Wang, *RSC Adv.*, 2016, **6**, 109061–109066.
35 X. Liu, J. Tong, J. Wang, S. Lu, D. Yang, H. Li, C. Liu and Y. Song, *J. Mater. Chem. C*, 2023, **11**, 4614–4622.
36 J. Jiang, S. Tu, R. Fu, J. Li, F. Hu, B. Yan, Y. Gu and S. Chen, *ACS Appl. Mater. Interfaces*, 2020, **12**, 33989–33998.
37 S. Kalani, R. Kohandani and R. Bagherzadeh, *RSC Adv.*, 2020, **10**, 35090–35098.
38 H. Kong, Y. Jin, G. Li, M. Zhang and J. Du, *Adv. Eng. Mater.*, 2023, **25**, 2201660.
39 J.-H. Lee, H.-J. Yoon, T. Y. Kim, M. K. Gupta, J. H. Lee, W. Seung, H. Ryu and S.-W. Kim, *Adv. Funct. Mater.*, 2015, **25**, 3203–3209.
40 Y. Jin, S. a. Xue and Y. He, *Adv. Mater.*, 2025, **37**, 2500076.
41 C. Li, P. M. Wu, S. Lee, A. Gorton, M. J. Schulz and C. H. Ahn, *J. Microelectromech. Syst.*, 2008, **17**, 334–341.
42 Y. K. Fuh, B. S. Wang and C.-Y. Tsai, *Sci. Rep.*, 2017, **7**, 6759.
43 A. N. Arshad, M. H. M. Wahid, M. Rusop, W. H. A. Majid, R. H. Y. Subban and M. D. Rozana, *J. Nanomater.*, 2019, **2019**, 5961563.
44 S. Saha, V. Yauvana, S. Chakraborty and D. Sanyal, *Mater. Today: Proc.*, 2019, **18**, 1450–1458.
45 Y. Cao, K. Zhu, J. Liu and J. Qiu, *Adv. Powder Technol.*, 2014, **25**, 853–858.
46 T. Lei, P. Zhu, X. Cai, L. Yang and F. Yang, *Appl. Phys. A: Mater. Sci. Process.*, 2015, **120**, 5–10.
47 L. Li, M. Zhang, M. Rong and W. Ruan, *RSC Adv.*, 2014, **4**, 3938–3943.
48 G. Wang, T. Liu, X.-C. Sun, P. Li, Y.-S. Xu, J.-G. Hua, Y.-H. Yu, S.-X. Li, Y.-Z. Dai, X.-Y. Song, C. Lv and H. Xia, *Sens. Actuators, A*, 2018, **280**, 319–325.
49 N. Chamankar, R. Khajavi, A. A. Yousefi, A. Rashidi and F. Golestanifard, *Ceram. Int.*, 2020, **46**, 19669–19681.
50 G. Chen, G. Chen, L. Pan and D. Chen, *Diamond Relat. Mater.*, 2022, **129**, 109358.
51 S. Wang, H.-Q. Shao, Y. Liu, C.-Y. Tang, X. Zhao, K. Ke, R.-Y. Bao, M.-B. Yang and W. Yang, *Compos. Sci. Technol.*, 2021, **202**, 108600.
52 A. Ahmed, N. A. Khoso, M. F. Arain, I. A. Khan, K. Javed, A. Khan, S. I. Memon, Q. Fan and J. Shao, *Polymer*, 2024, **16**, 1781.